Chapter 4

Co-MOF derived from Cobalt salt and Anthranilic acid for enhanced oxygen evolution reaction (OER)

4.1 Introduction

Energy is a very fundamental and essential thing for every human being. As the population increases day by day, the sophistication of human civilization and the energy requirement also increases in proportion to that. Non-renewable energy sources (coal, petroleum, natural gas) fulfil this demand widely, but these energy sources are not sustainable, they are depleting continuously [161]. Also, global warming is the biggest threat which is produced by the frequent use of these energy sources. Therefore, there is an urgent need to go for renewable energy sources like solar energy, wind energy, geothermal energy, production of H_2 and O_2 through water splitting etc. as they generate clean and zero carbon emission energy which is environmentally friendly, also not limited [162, 163]. Among them, water-splitting electrocatalysis is the most productive and sustainable approach for producing clean and green energy [164, 165].

Electrocatalysis of water comprises two half-reactions, hydrogen evolution reaction (HER) and oxygen evolution reaction (OER) in which HER is a cathodic process and OER is an anodic process. To generate clean and green energy, electrochemical energy conversion and storage (ECS) systems are imperative. Water electrolyzers, fuel cells and metal-air batteries are widely operative ECS devices, and in these systems, OER is an essential process and a key half-cell reaction of water splitting [166, 167]. It is a four-electrons and four protons coupled electrochemical reaction necessitating a very high overpotential. This causes the sluggish kinetics of the OER in acidic and basic mediums ($4OH^- \rightarrow 2H_2O + O_2 + 4e^-$ in base and $2H_2O \rightarrow 4H^+ + O_2 + 4e^-$ in acid) [124]. In comparison to the acidic medium, in the alkaline medium, adsorption of a large amount of OH^- takes place at active sites of the catalyst surface to form the active OH^- which

gives rise to a very slow OER process [168]. Therefore, highly efficient and robust electrocatalysts such as RuO_2 and IrO_2 are essential to facilitate this reaction. Although they are the most effective and state-of-the-art electrocatalysts for OER, their high cost, inadequacy, and poor stability hindered them from putting into practice on a large scale [169, 170]. Thus, we need to develop highly efficient electrocatalysts for OER keeping in mind the cost-to-performance ratio needed for commercialization. Transition metal-based materials as an electrocatalyst have been explored extensively in recent years as they are earth-abundant and low-cost. No-noble transition metals Fe, Co, Ni, Mn, Cu, and their oxides [171, 172], and mixed-metal oxides [173, 7, and 88] have been gaining ample attention because of their high activities and robust stability. Despite these interesting features, also they possess several drawbacks for the implementation at a large scale. The low electrical conductivity, change in the volume during cycling, reduced charge transfer, sensitivity to pH and insufficient catalytic activity constrained their applications in electrochemical processes [174].

Besides the transition metal oxides, a plethora of materials including carbon allotropes [175], conducting polymers, and their composites [20] have also been employed for OER, but still do not meet the industry requirements. Metal-organic frameworks (MOFs) are a family of materials in which metal and organic ligands are attached through coordination bonds. These materials act as the link between the inorganic and organic materials. These are crystalline coordination networks and possess very interesting properties such as tunable porosity, high surface area, and elasticity in the functionalization with various ligands and metal centres [88, 176-178]. Such excessive properties are accountable for the potential applications of MOFs in varieties of fields such as gas storage and separation, catalysis, sensors, water treatment and drug delivery [179, 180, 95, and 81]. MOFs also emerge as a promising substitute for noble metal-based electrocatalysts in

water-splitting electrocatalysis. The available active surface area of MOFs can significantly decrease the diffusion distance of the charge carriers to the reactants in electrocatalysis. Due to the distinctly approachable metal-ligand junctions, the interfacial electronic coupling interaction in MOFs is achieved, enhancing the redox reaction's efficiency in the water-splitting process [181- 183]. The high density of closely located sites allows the reactants to easily cross the free energy path, converting it into the desired products. Thus, MOFs with desirable electrocatalytic functionality are achieved by linking specific redox-active metal ions and organic ligands, providing a suitable path to connecting the electroactive components.

Due to the diversity in metal centres and organic linkers, thousands of MOFs have been synthesized, and still, research is increasing exponentially. The topology of the resulting MOF is mainly governed by the geometry of the organic ligands [81]. At the same time, functional groups attached to the organic moiety and redox active metal centres contribute to the catalytic performance of the MOF. Herein, we synthesized a Co-MOF using the Anthranilic acid (AA) as an organic linker, and Co^{2+} as a metal node from a simple precipitation method and rose-like morphology is obtained. Because of amine ($-NH_2$) and carboxylate ($-C=O-O^-$) functional groups, AA possesses a higher electron density which facilitates the bonding of Co^{2+} to AA very easily through coordination bonds. At the same time when the reaction occurs, it grows and emerges into a flower-like morphology constituting the sheet-like petals. No such reports are available for this type of morphology of Co-MOF, as per our knowledge. As-synthesised Co-MOF is confirmed by various characterisation techniques such as UV-Vis, FT-IR, XPS and mass spectroscopy and the structure is optimised through DFT analysis.

4.2 Results and discussion

4.2.1 Structural analysis

4.2.1.1 XRD and UV-Vis analysis

To investigate the compositions and average crystallite size of as-synthesized Co-MOF crystals, powder XRD patterns were recorded at room temperature using Cu-kα1 radiation (wavelength, λ=1.54059 Å). Figure 1(a) represents the XRD patterns for Anthranilic acid and Co-MOF. All the diffraction peaks of Co-MOF are found to be well-matched with the pattern with JCPDS No. 00-045-1729. Now, the average size of crystalline domains which diffract coherently has been estimated using the Debye-Scherrer formula (Eq. 2.6). The average crystallite size for Co-MOF is found to vary from 16-58 nm, while the crystallite size calculated from the Williamson-Hall plot (supporting information) is about 40.6 nm which is in accordance with the Scherrer outcomes. Thus, XRD patterns evidenced the successful synthesis of crystalline Co-MOF through the hydrothermal process with negligible defect sites.

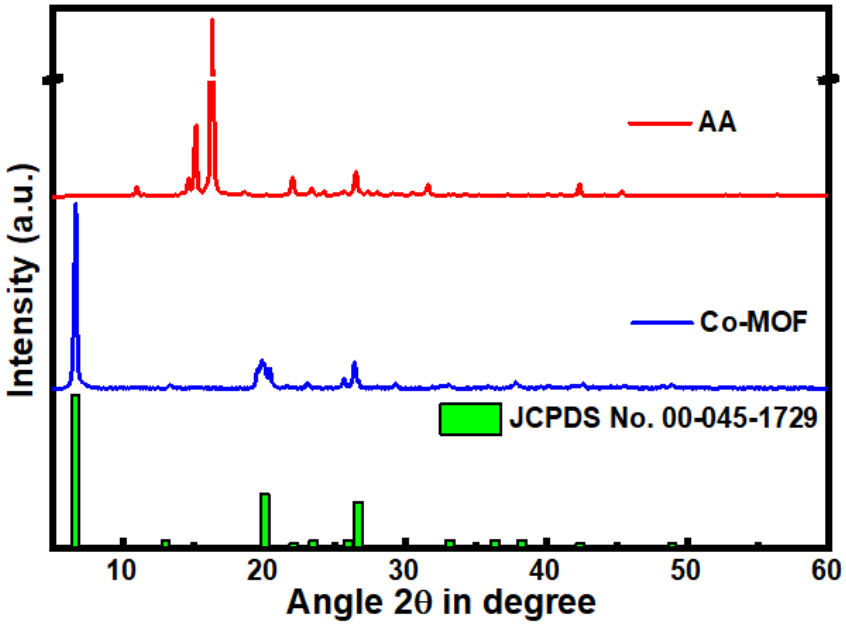

Figure 4.1 Powder X-Ray diffraction pattern for Anthranilic acid (AA) and Co-MOF.

Next, to study the optical and band-gap properties of as-synthesized Co-MOF, we recorded the UV-Vis. spectra at room temperature using a non-polarised light source in diffuse reflectance mode. The absorption band edge for Anthranilic acid was nearly 398 nm, while after MOF formation with cobalt, there has been a hypsochromic shift of ~61 nm in spectral band position (337 nm). After that, to determine the energy needed for photoexcitation of the valence band electrons to the conduction band, we have applied the Kubelka-Munk (K-M) theory for direct allowed type band transition and perfect diffuse scattering from samples, as

$$(\alpha h\nu)^2 = C_2(h\nu - E_g) \qquad \text{(Eq. 4.1)}$$

Here, C_2: proportionality constant, α: absorption coefficient, and from the $(\alpha h\nu)^2$ vs photon energy $(h\nu)$ plot we have estimated the optical gap (E_g). The optical gap in CoMOF was found to be higher (3.68 eV) as compared to the Anthranilic Acid (3.11eV). As MOF formation causes an extended π-conjugation, a decrease in the optical gap was expected, however, a distorted tetrahedral structure of Co-MOF hinders the intra MOF π-π stacking and a lower optical gap has been observed.

4.2.1.2 FT-IR analysis

The IR spectra of AA showed stretching frequency at 3474 cm^{-1} due to the O-H group in the carboxylic acid (COOH) and a doublet at 3375 and 3324 cm^{-1} due to amino (NH_2) group (asymmetrical and symmetrical stretching). While, in Co-MOF, O-H stretching of the carboxylic group disappeared entirely due to the deprotonation of the carboxylic group during the synthesis with aqueous NaOH [Figure 4.9(a)]. The stretching vibration for the N-H_2 group appeared at 3308 and 3402 cm^{-1} and N-H bending appeared at 1614 cm^{-1}. The signals appeared in AA at 1671 and 1420 cm^{-1} due to asymmetric and symmetric stretching vibration of the carboxylate group (COO^-) whereas in Co-MOF

these bands are shifted towards lower frequency (1615 and 1410 cm^{-1}) which supports the complexation of the carboxylic group of AA with Co. Along with that C-N (1245 cm^{-1}) and C-O (1160 cm^{-1}) signals in AA also shifted to a lower frequency in Co-MOF (as 1615 and 1410 cm^{-1}) which supports the complexation of the carboxylic group of AA with Co. Along with that C-N (1245 cm^{-1}) and C-O (1160 cm^{-1}) signals in AA also shifted to a lower frequency in Co-MOF (as 1037 and 952 cm^{-1}, respectively) due to the bond formation with Co. The bonding of Co with oxygen (Co-O) and nitrogen (Co-N) appeared at 420 and 562 cm^{-1}, respectively. All these findings confirm the successful complexation of Co with AA in Co-MOF.

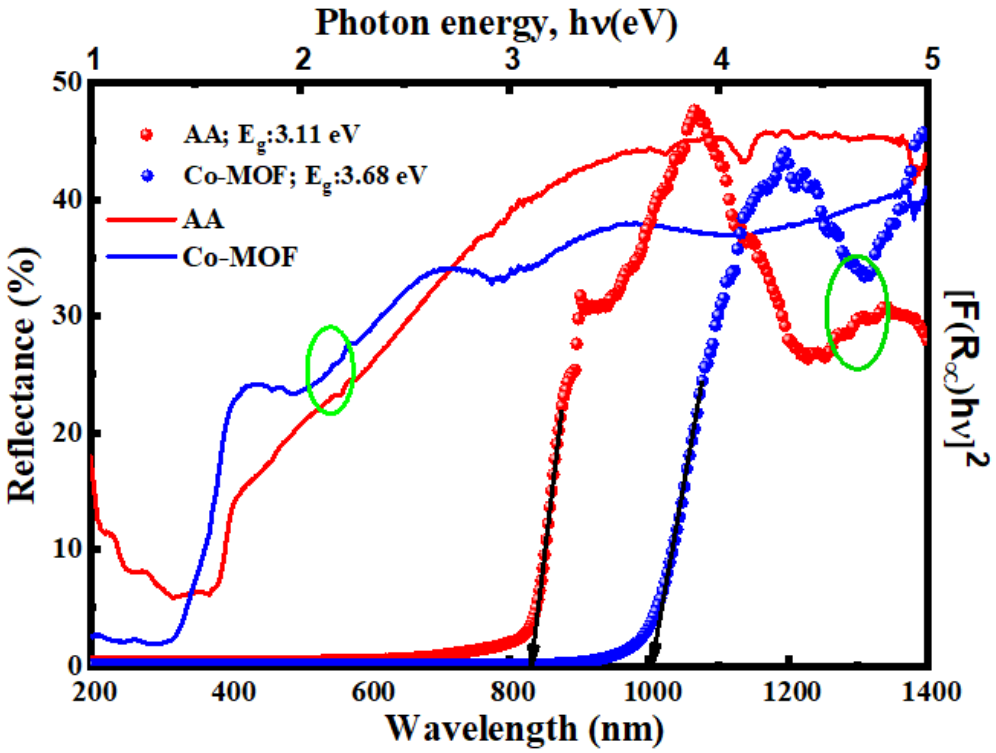

Figure 4.2 UV-Vis. diffuse reflectance spectra measured at room temperature and their corresponding K-M function plot.

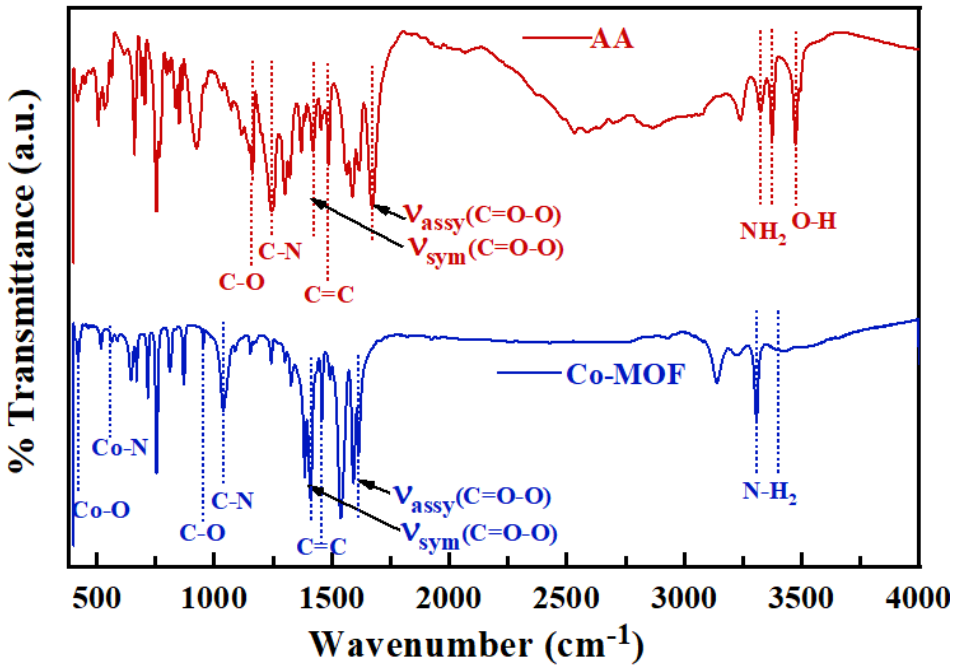

Figure 4.3 FT-IR spectra of Anthranilic acid and Co-MOF.

4.2.1.3 XPS analysis

Subsequently, the chemical composition of Co-MOF is analysed by XPS and for the comparison, XPS of Anthranilic acid is also shown in Figure 4.4. The full survey spectrum of Co-MOF is shown in Figure 4.4(a), which shows the existence of the elements Co, C, N and O. The core level spectrum of Co_{2p} consists of two spin-orbit doublets along with the satellite peaks. The signals observed at 779.8 eV (Co $2p_{3/2}$) and 796.3 eV (Co $2p_{1/2}$) corresponds to Co^{2+}. Also, the satellite peaks at 785 eV (Co $2p_{3/2}$) and 801.8 eV (Co $2p_{1/2}$), further confirming the presence of Co^{2+} and it is consistent with previous findings [88]. As shown in Figure 4.5(b), the core level spectrum of C_{1s} exhibited four peaks at 284.2, 285.4, 287.8 and 290.8 eV due to the C-C (C=C), C-N, C=O and O-C=O functional moieties. Further, the O_{1s} spectrum [Figure 4.5 (c)] is deconvoluted into three peaks at 530.8, 531.5 and 532 eV for Co-O, C=O and O-C=O groups affirming the bonding of Co with AA, and this is also further supported by the spectrum of N_{1s} [Figure

4.5(d)] where the peak is observed for Co-N bond (399.8 eV). The other two peaks in N_{1s} are designed for C-N (398.9 eV) and NO_2 (406.4 eV) groups [184, 185].

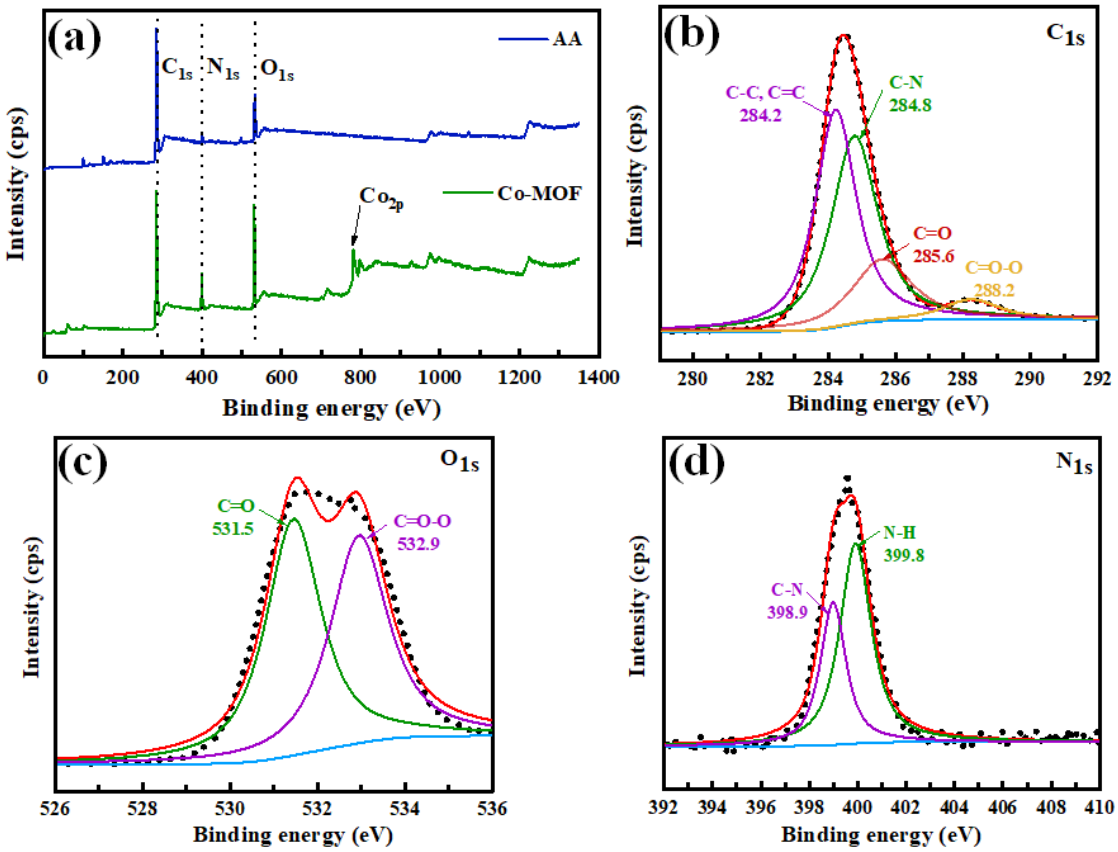

Figure 4.4 (a) Full survey XPS spectrum of AA and Co-MOF, high-resolution XPS spectrum of (b) C_{1s}, (c) O_{1s}, and (d) N_{1s} in Anthranilic acid (AA).

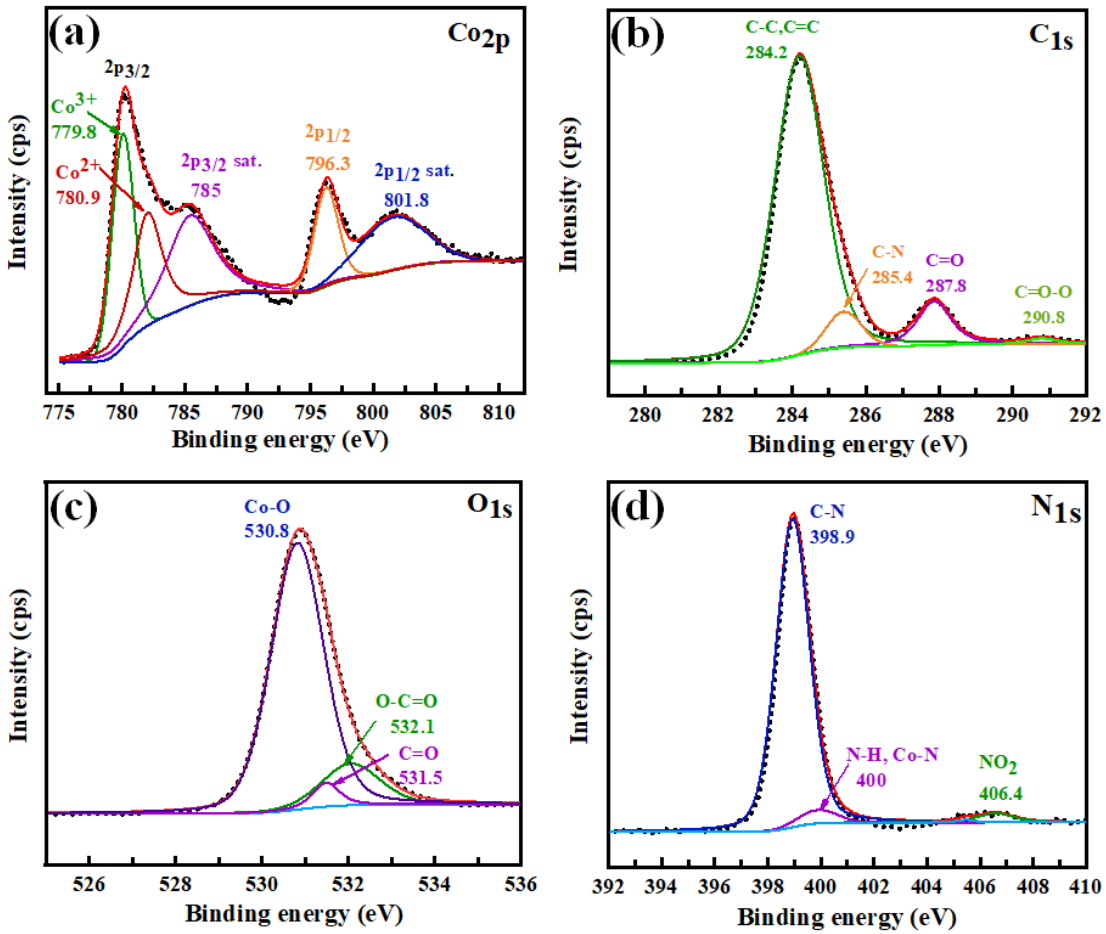

Figure 4.5 The core level deconvoluted spectrum of (a) Co_{2p}, (b) C_{1s}, (c) O_{1s} and (d) N_{1s} in Co-MOF.

4.2.2 Mass-spectrometry

The Mass spectrum is a plot of intensity with respect to the mass-to-charge ratio (m/z). The spectrum shows characteristic fragmentation patterns and by tallying these patterns with known masses, we can recognise the atoms or molecules in the sample. The most intense ion shows the highest intensity and it is stated as the base peak [186]. In Figure 4.6 the peak corresponding to m/z =329.17 shows the highest intensity among others (equivalent to the molecular weight of Co-MOF).

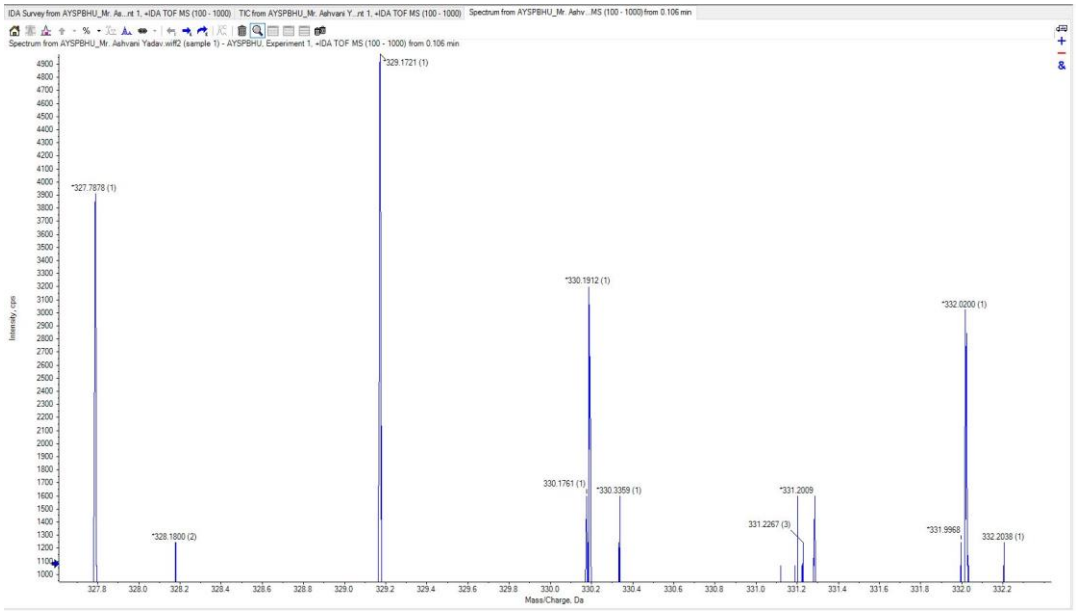

Figure 4.6 Mass spectra of Co-MOF.

4.2.3 DFT analysis

In order to investigate the energy minimized stable structure of Co-MOF, its HOMO (highest occupied molecular orbital) and LUMO (lowest unoccupied molecular orbital) positions theoretically for establishing its role towards OER application, we have implemented the density functional theory (DFT) using the Gaussian G09 software. The Co-MOF structure was initially optimized using the diffuse basis set (6-31G) and B3LYP as an optimal computation cost to the level of accuracy ratio for the 3D gaseous model, and then the optimized structure was used for further calculation. Thus, all quantum chemical parameters like dipole moment, E_{HOMO}, E_{LUMO}, absolute electronegativity (χ) were determined for stable Co-MOF and tabulated in Table 4.1. Molecular orbitals corresponding to the optimized structures are represented having iso value 0.02 in Figure 4.7. Now, according to the Koopman's theory [187], the electron affinity (A) and the ionization potential (I) of Co-MOF could be related as $A = -E_{LUMO}$ and $I = -E_{HOMO}$, while the absolute electronegativity (χ) can be determined as $\chi = \left(\frac{I+A}{2}\right)$.

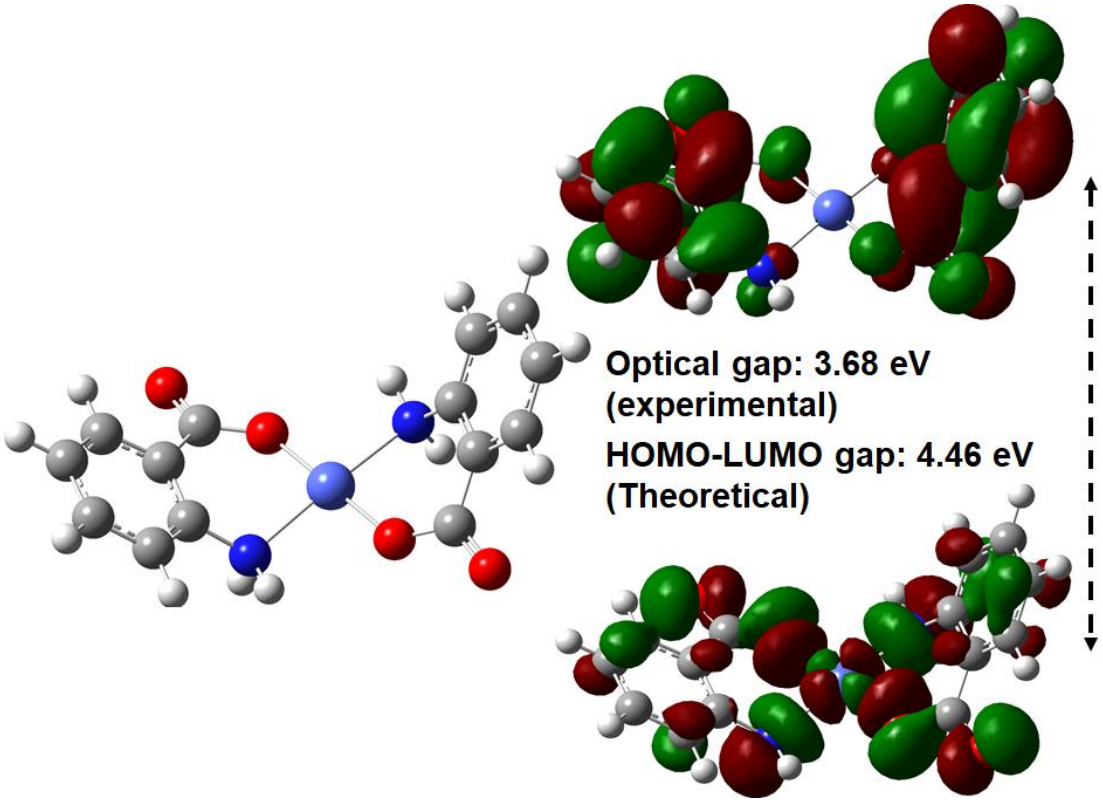

Figure 4.7 Optimized structure of Co-MOF and its HOMO-LUMO.

Table 4.1 Structural parameters for optimised Co-MOF.

Electronic Parameters	Co-MOF
E_{HOMO} (eV)	-6.7467
E_{LUMO} (eV)	-2.2861
$\Delta E_{LUMO-HOMO}$ (eV)	4.4606
μ (D)	1.0901
χ (eV)	4.5164

Apart from the Scherrer formula, we have used the Williamson-Hall (W-H) relation [188] to calculate the average crystallite size (D) and lattice strain as follows,

$$\frac{\beta Cos\theta}{\lambda} = \frac{1}{D} + \frac{\varepsilon Sin\theta}{\lambda} \qquad \text{(Eq. 4.2)}$$

where, λ denotes the wavelength of X-ray (1.54059 Å) used, β is the integrated peak-width at half maxima, ε represents the micro-strain present in the Co-MOF crystals.

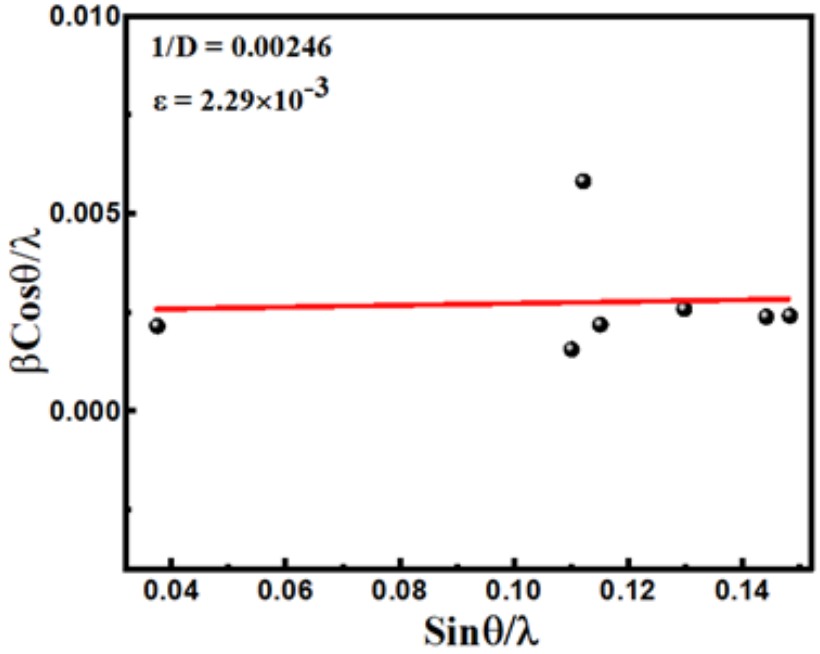

Figure 4.8 Williamson-Hall plot corresponding to Co-MOF.

4.2.4 Proposed reaction mechanism and morphological analysis of Co-MOF

Co-MOF flowers are directly grown in the solution by a facile precipitation method without using any substrate. Initially, with the addition of NaOH in Anthranilic acid solution, carboxylic groups (COOH) deprotonate [Figure 4.9(a)]. Carboxylate (COO^-) and amino (NH_2) groups both have lone pairs of electrons, which facilitates the linkage of Co^{2+} through coordination bonds as the cobalt salt solution is added gradually into it. Co^{2+} has vacant 4s and 4p orbital, and both groups (COO^- and NH_2) act as weak field ligands; therefore, the Co-MOF might have resulted in a tetrahedral geometry, but it adopted a distorted tetrahedral structure due to the chelation. The optimised structure getting through DFT analysis also reinforces the above mechanism. As the nucleation begins rapidly everywhere in the reaction mixture, the nucleation sites of Co-MOF are created. In spite of the distorted tetrahedral structure of Co-MOF, multiple Co-MOFs are

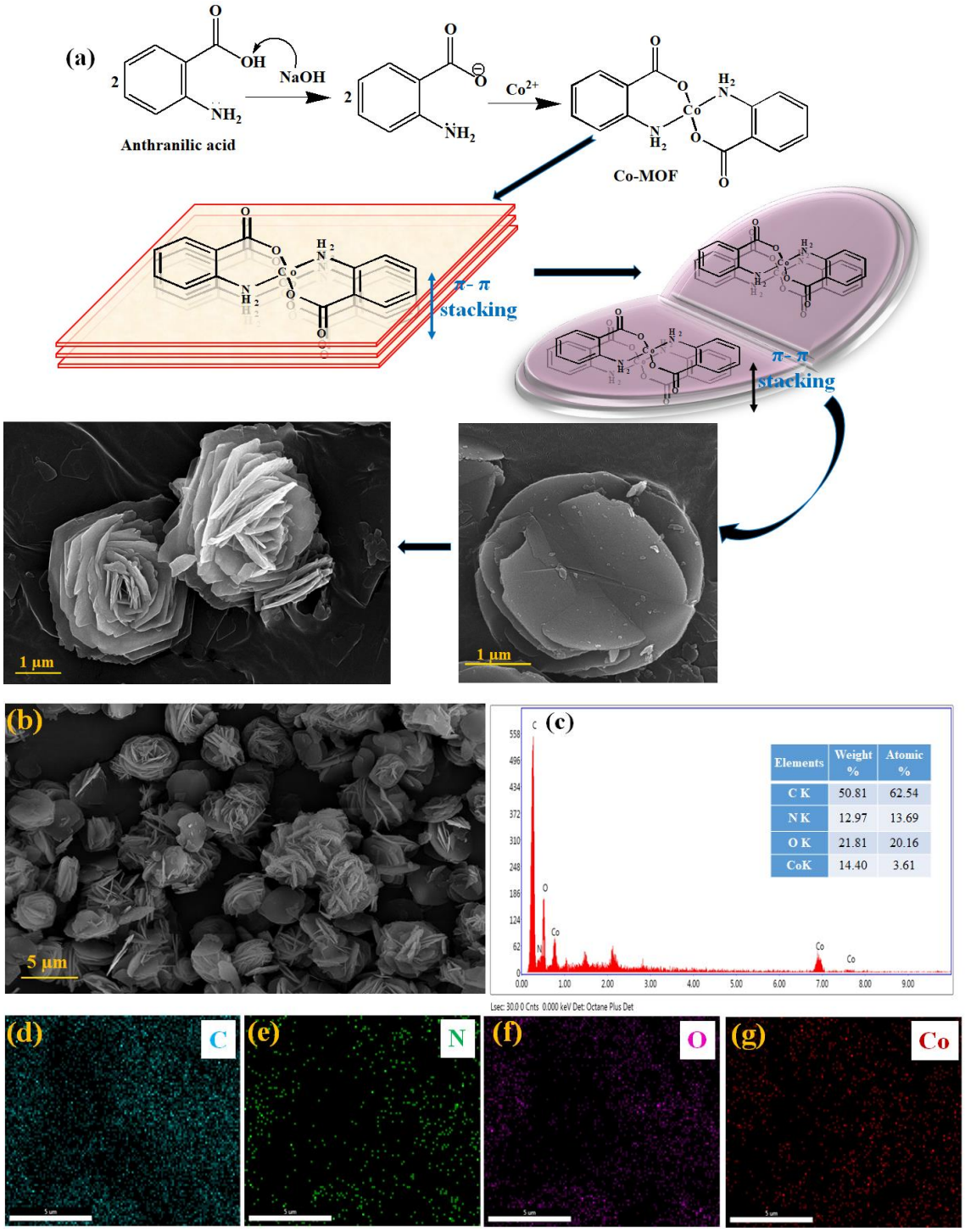

Figure 4.9 (a) Schematic representation of the mechanism of reaction and growth process in flower structure of Co-MOF, (b) FE-SEM image, (c) EDX spectrum, and from (d) to (g) elemental mapping of a selected area of Co-MOF.

arranged on one another through π-π stacking due to the delocalized pi electrons of benzene rings. Through this, sheets are developed in a folded manner like petals and finally emerge into a flower [Figure 4.9(a)]. As can be seen in Figure 4.9(b), the flowers

are distributed uniformly throughout the sample, and micron size of the flowers are grown in the solution comprising the average size of the flower ~4 µm and the average length of the petals ~800 nm (Figure 4.10). EDAX and elemental mapping display the distribution of the elements Co, C, N and O.

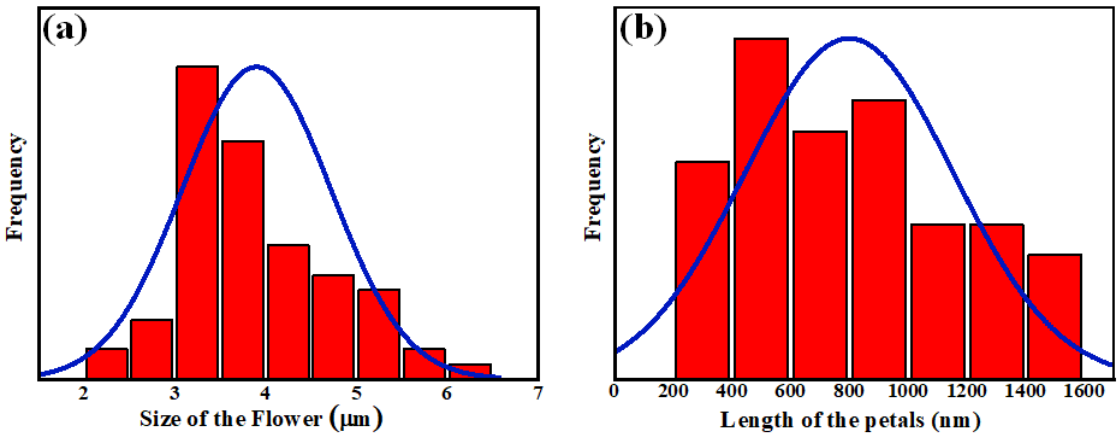

Figure 4.10 Distribution plots for the (a) size of the flower and (b) petals length in Co-MOF.

4.2.5 BET measurement

BET and BJH methods are employed to evaluate the surface area, pore size, pore volume, and pore size distribution of Co-MOF. Figure 4.11 presents the N_2 adsorption and desorption isotherm and respective pore size distribution. The isotherm plot resembles Type IV with hysteresis loops H3 having the mesoporous nature of the particles and is in good agreement with earlier reported metal complexes [7, 88]. The specific surface area and pore volume of the synthesized Co-MOF have been analysed from BET measurement, and the values are 17.9 m^2g^{-1} and 0.169 cm^3g^{-1}, respectively. The BJH pore size distribution plot is shown in [Figure 4.11(b)], having an average pore diameter of 37.74 nm.

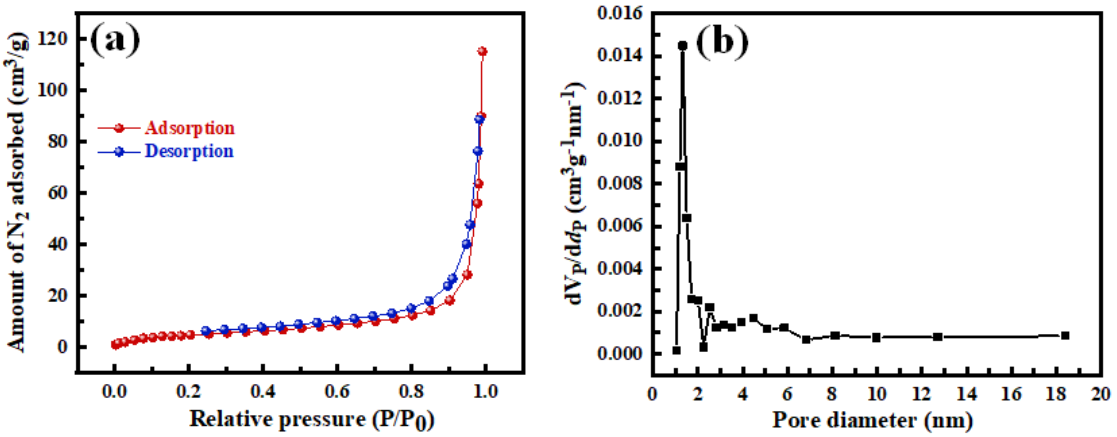

Figure 4.11 (a) N_2 adsorption-desorption isotherm and (b) pore area distribution plot of Co-MOF.

4.2.6 OER study and stability test

The electrocatalytic performances of the catalysts towards OER are examined by LSV, Tafel slope and EIS (electrochemical impedance spectroscopy) and compared with the commercially available RuO_2. All the measurements are carried out in 0.5 M KOH (pH=13.7). Linear sweep voltammetry (LSV) was performed from 1.0 to 2.0 V vs. RHE at 5 mVs^{-1}. Impedance measurement was done at 5 mV amplitude in the frequency range from 10^5 to 0.01 Hz using EIS. [Figure 4.12(a)] shows the LSV plots of bare GC, Co-MOF and RuO_2. Co-MOF has a higher current density even with RuO_2, indicating low overpotential to reach 10 $mAcm^{-2}$ current density ($Co\text{-}MOF_{(Overpotianl\ at\ 10)}$ = 0.52 V vs. $RuO_{2(Overpotianl\ at\ 10)}$ = 0.6 V vs RHE). At 50 mA cm^{-2}, it exhibits the overpotential 0.61 V vs RHE. [Figure 4.12(b)] shows the corresponding Tafel plot. The Tafel slope is a quantitative measure to evaluate the activity of the catalysts and is also a constituent of determining the reaction mechanism. It is calculated by the linear fitting of Eq 1.40. Co-MOF has a lower Tafel slope of 58 $mVdec^{-1}$ than RuO_2 (68.8 $mVdec^{-1}$), suggesting that for every 10-fold increase in the current, it requires a lesser overpotential than RuO_2. Further, EIS measurement is another important gauge to check the OER performance of the catalysts by measuring the charge transfer resistance (R_{ct}). It is a tool for the complete

characterization of the electrode and electrolyte interface and corresponding process [112]. The Nyquist plot of Co-MOF is presented in [Figure 4.12(c)], showing the R_{ct} value~380 Ω cm^2 (as the curve touches the x-axis).

The oxygen evolution reaction occurs through adsorption and discharge of the OH^- at the active site of the catalyst (S) [21]. Through this, a number of intermediates (S-OH, S-O, S-OOH, and S-OO) are formed at the catalyst surface, followed by the formation of O-O bond (O_2) as given the reaction mechanism in section [1.3.1.1(a)(ii)].

Further, to quantify the actual surface area of the catalyst, which is catalytically active, C_{dl} is calculated. Electrochemical active surface area (ECSA) is directly proportional to the C_{dl}. To estimate the C_{dl} value, as shown in Figure 4.11, cyclic voltammetry of the Co-MOF is performed in the non-faradic potential from 1.12 to 1.32 V vs. RHE at varying scan rates from 10 to 100 mVs^{-1}. Then, the difference of the anodic and cathodic current density ($\Delta j_{1.22} = j_a - j_b$) versus scan rate is plotted as can be seen in [Figure 4.12(d)]. The C_{dl} value is calculated as half of the linear slope of the above-linear fitted graph.

Durability and operational stability are critical parts of the catalyst to prove its integrity as an electrocatalyst. The current stability at a particular overpotential for a long time is an important criterion to gauge the catalyst's performance. Therefore, the stability of the Co-MOF is examined by the chronoamperometry process in which continuous OER is performed on the application of a static overpotential of 500 mV vs. RHE for 15000 seconds [Figure 4.12 (e)]. After 6000 seconds, it shows the static behaviour of the current. The changes in the current at the early stages of the measurement are expected due to the diffusion of the electrolytes. After 15000 seconds, LSV is recorded [Figure 4.12(f)], and a nearly comparable current is observed, having the same onset potential.

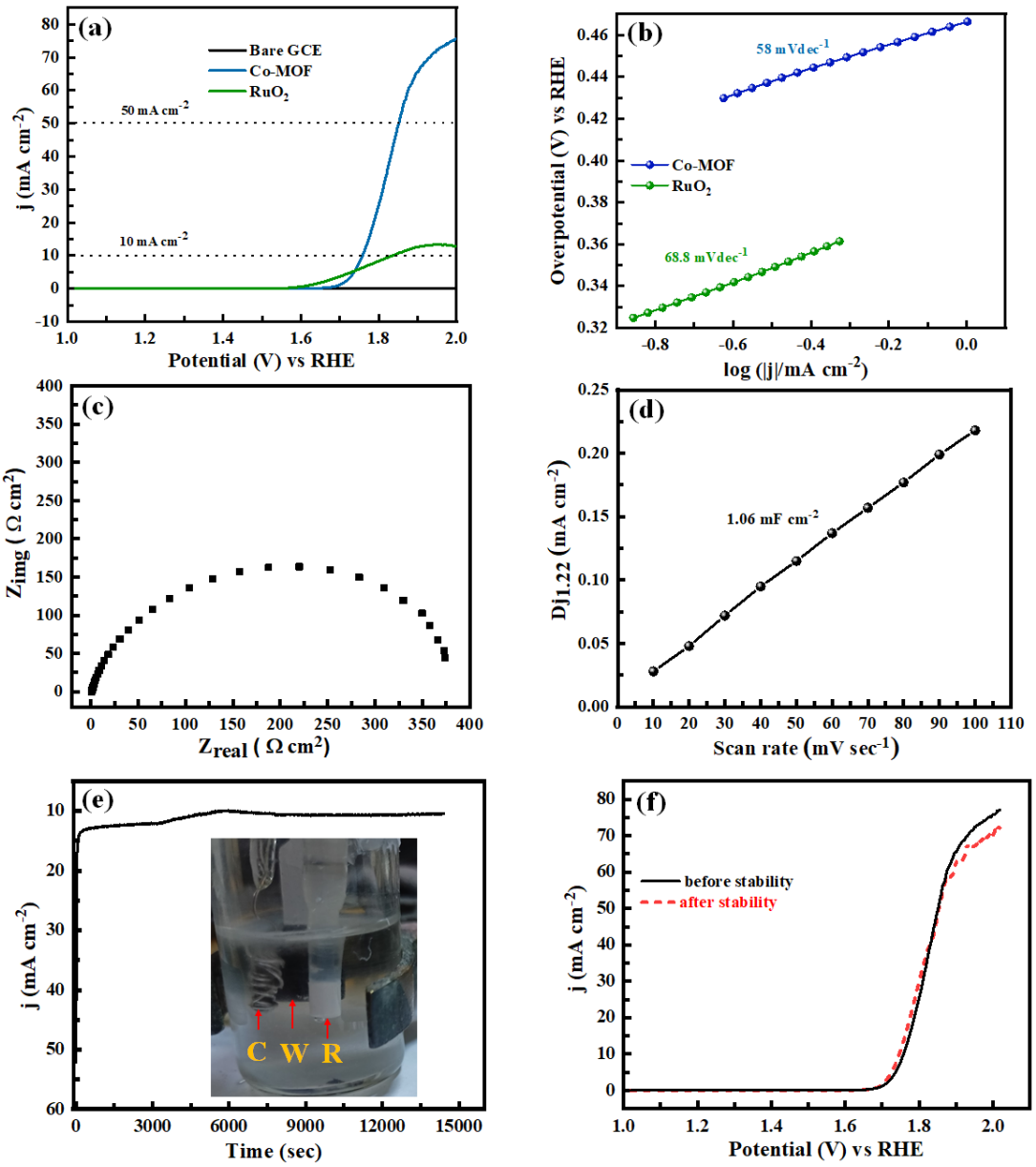

Figure 4.12 (a) LSV polarization curve at 5 mVs^{-1}, (b) Tafel slopes, (c) Nyquits plot, (d) double layer capacitance (Cdl) calculation at 1.22 V vs RHE of Co-MOF and RuO_2 in 0.5 M KOH, (e) chronoamperometry of Co-MOF for 15,000 seconds at a static overpotential of 500 mV in 0.5 M KOH, and (f) response of OER current before and after stability. The cell configuration (R-reference, C-counter, and W-working electrode) for the chronoamperometry measurement is shown in inset [Figure 1.2(e)].

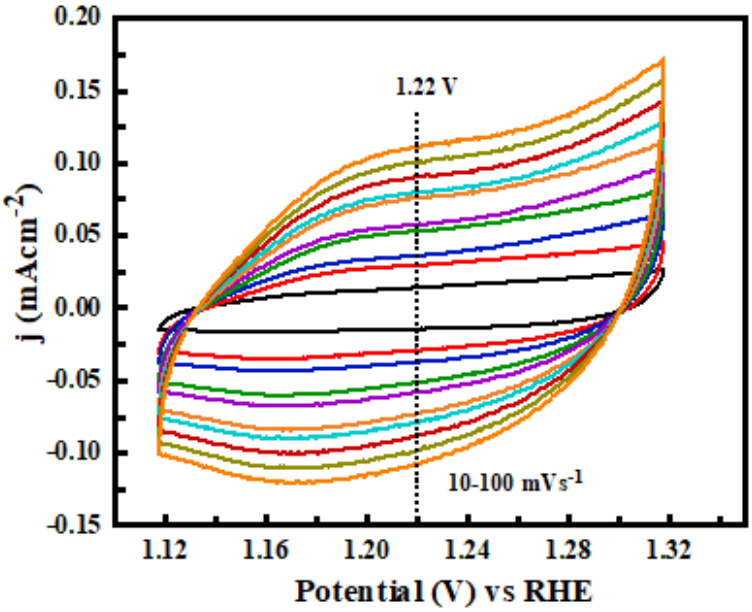

Figure 4.13 Cyclic voltammetry (CV) of (a) Co-MOF at varying scan rates from 10 to 100 mV s^{-1}.

4.3 Conclusions

In conclusion, we have synthesized a beautiful rose-like structured Co-MOF using cobalt salt as a metal node and Anthranilic acid as an organic linker, by a very facile precipitation approach. The characterization techniques well explain the complexation of cobalt ions with Anthranilic acid and the optimized structure of Co-MOF is obtained through the theoretical study using DFT. Then, as synthesized Co-MOF is tested for OER performance. It shows the overpotential of 520 mV at 10 $mAcm^{-2}$ current density with Tafel slope 58 $mVdec^{-1}$ and C_{dl} value is 1.06 $mFcm^{-2}$. Further, the stability test is performed by the CA for 15000 seconds at a static overpotential of 500 mV and it shows almost equal current density as before with no significant change in the onset potential.